

Chapter 5

2D field data applications

In chapter 4, using synthetic examples, I showed how the regularized joint data-domain and image-domain inversion methods developed in chapter 3 overcome different time-lapse imaging challenges. In this chapter, I apply joint image-domain inversion to subsets of a North Sea field time-lapse data set. These two-dimensional marine streamer data are extracted from three-dimensional seismic surveys acquired as part of Statoil's time-lapse seismic monitoring project at the Norne field. Recall that in chapter 2, I used the preprocessed, pre-stack time-migrated (PSTM) images obtained from four years (2001, 2003, 2004 and 2006) to demonstrate applications of conventional post-imaging time-lapse cross-equalization methods.

In this chapter, I utilize two raw data sets recorded in 2006 and 2008 to demonstrate how different preprocessing steps improve time-lapse amplitude information and condition the data for inversion. Data preprocessing is important to ensure that as nearly as possible, the data satisfy the assumptions made in chapter 3. If these assumptions are not satisfied, the inversion methods developed in this dissertation cannot give reliable results. First, to satisfy the primaries-only assumption, multiples and other uncorrelated noise must be removed. Then, bulk amplitude difference between the data sets (e.g., due to differences in acquisition instruments), must be taken into account. Finally, all image points between the baseline and monitor images must

be collocated. In addition, I show that that linearized inversion can improve time-lapse images in conventional acquisition geometries. Furthermore, I demonstrate that this method can be used to attenuate obstruction artifacts in time-lapse images.

As discussed in chapter 2, the Norne field is located in the Norwegian sector of the North Sea. A summary of the field geology and production history is presented in chapter 2. Osdal et al. (2006) and Aarre (2008) provide more detailed description of the Norne field geology, the production history, the monitoring objectives, the time-lapse seismic data acquisition and processing, and some interpretation of the time-lapse seismic responses observed in the field. For this study, the baseline data were acquired in 2006, whereas the monitor data were acquired in 2008. The shots and receivers are binned to 25 m spacings with a maximum offset of 3,200 m. Figure 5.1 shows a portion of the raw baseline data set.

This chapter is divided into two broad sections:

- First, using the complete baseline and monitor data sets, I show how different preprocessing steps and joint image-domain inversion improve time-lapse amplitude information. In this example, the baseline and monitor data sets have similar geometries.
- Second, I simulate an obstruction in the monitor data with a gap 400 m wide. In this example, except at the obstruction where no sources or receivers are present in the monitor, the baseline and monitor data sets have similar geometries.

Figure 5.2 shows the full migrated baseline and monitor stacked sections. To obtain these images, I migrate the data sets with a shot-profile one-way wave-equation algorithm using 290 frequencies up to 40 Hz. Note that the subsurface geology along this section of the field is relatively simple, with predominantly horizontal reflectors. The target area for inversion is between 1,500 m and 4,000 m along the vertical (depth) axis and between 0 m and 11,100 m along the horizontal (common-midpoint) axis. Henceforth, I show the results only for this target area. In this chapter, all inversion results are obtained using the RJMI formulation.

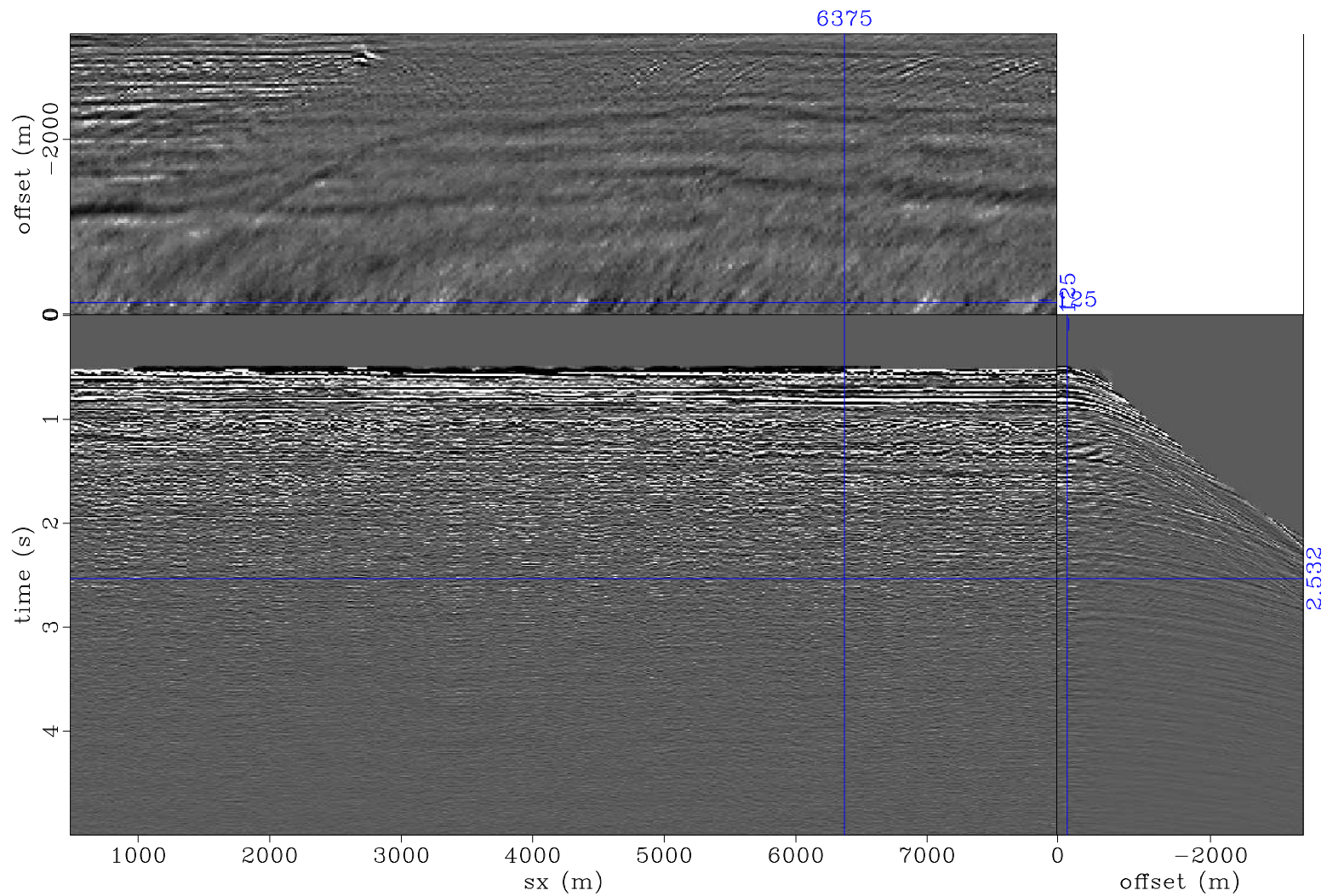


Figure 5.1: A portion of the raw two-dimensional streamer data from the Norne 2004 (baseline) data set. [CR] chap5/. dmhl-dat-2759-b4

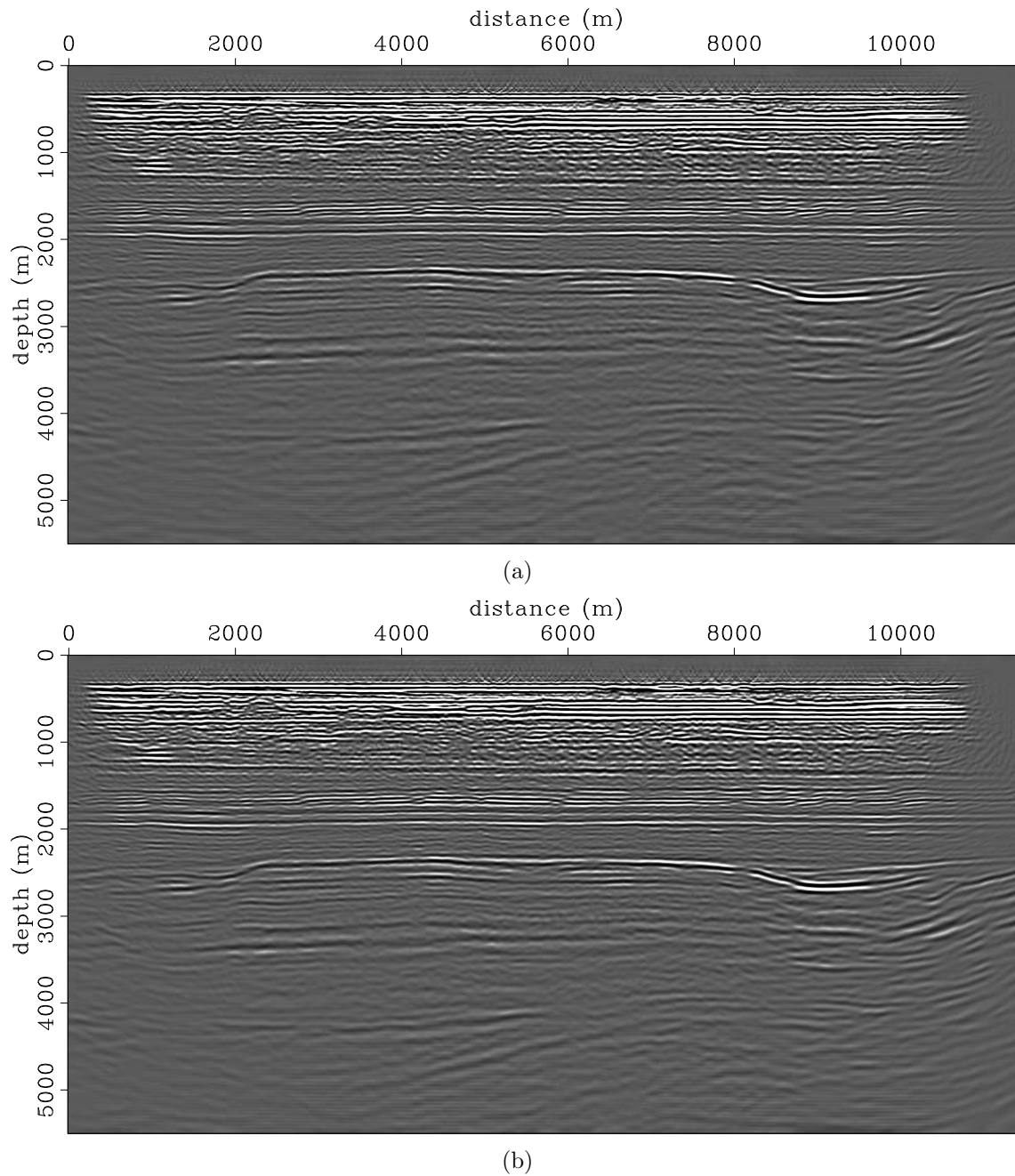


Figure 5.2: Raw baseline (a) and monitor (b) stacked images. Note that, along this section, the geology is relatively simple, with predominantly horizontal reflectors. The reservoir is located at approximately 2600 m depth. [CR]

chap5/. raw-2759-full-g-06,raw-2759-full-g-08

Example I: Inversion of complete data sets

In this example, I present the processing and inversion of the complete baseline and monitor data sets. Figure 5.3 shows the migrated pre-stack images obtained from the raw baseline and monitor data sets.

In Figure 5.3, note that the events showing significant curvature in the pre-stack image are multiples, whereas the horizontal events are the correctly migrated horizontal primaries. Because of small differences in the characteristics of multiples between the baseline and monitor surveys, if they are not attenuated, the multiples will contaminate the time-lapse amplitude information of interest. Figure 5.4 shows the pre-stack baseline and monitor images after high-resolution multiple attenuation. I perform this multiple-attenuation procedure using a parabolic Radon operator (Trad et al., 2003) and a robust conjugate-directions solver (Claerbout and Fomel, 2011).

First, I derive an inverted Radon model that predicts all events in the CMP-sorted data sets. Then, I determine a range of curvature parameters that contains all primary events. Seismic events predicted by the Radon model outside this range of curvature parameters are then subtracted from the recorded data sets. In this preprocessing step, I use the same parameters for both the baseline and the monitor data sets.

Note that several artifacts that are present in the migrated images obtained from the raw data (Figure 5.3) have been attenuated in the migrated images obtained from the preprocessed data (Figure 5.4). As mentioned above, and as I will show later in this section, differences between multiples of different surveys contaminate the time-lapse image.

Using images obtained from the preprocessed data, I estimate and apply a bulk amplitude correction to the monitor data. Differences in energy between seismic images may be caused by differences in the acquisition instruments for the different surveys. Prior to inversion, bulk amplitude differences between the baseline and monitor images must be removed. This ensures that such amplitude differences do not mask production-related amplitude differences between the images.

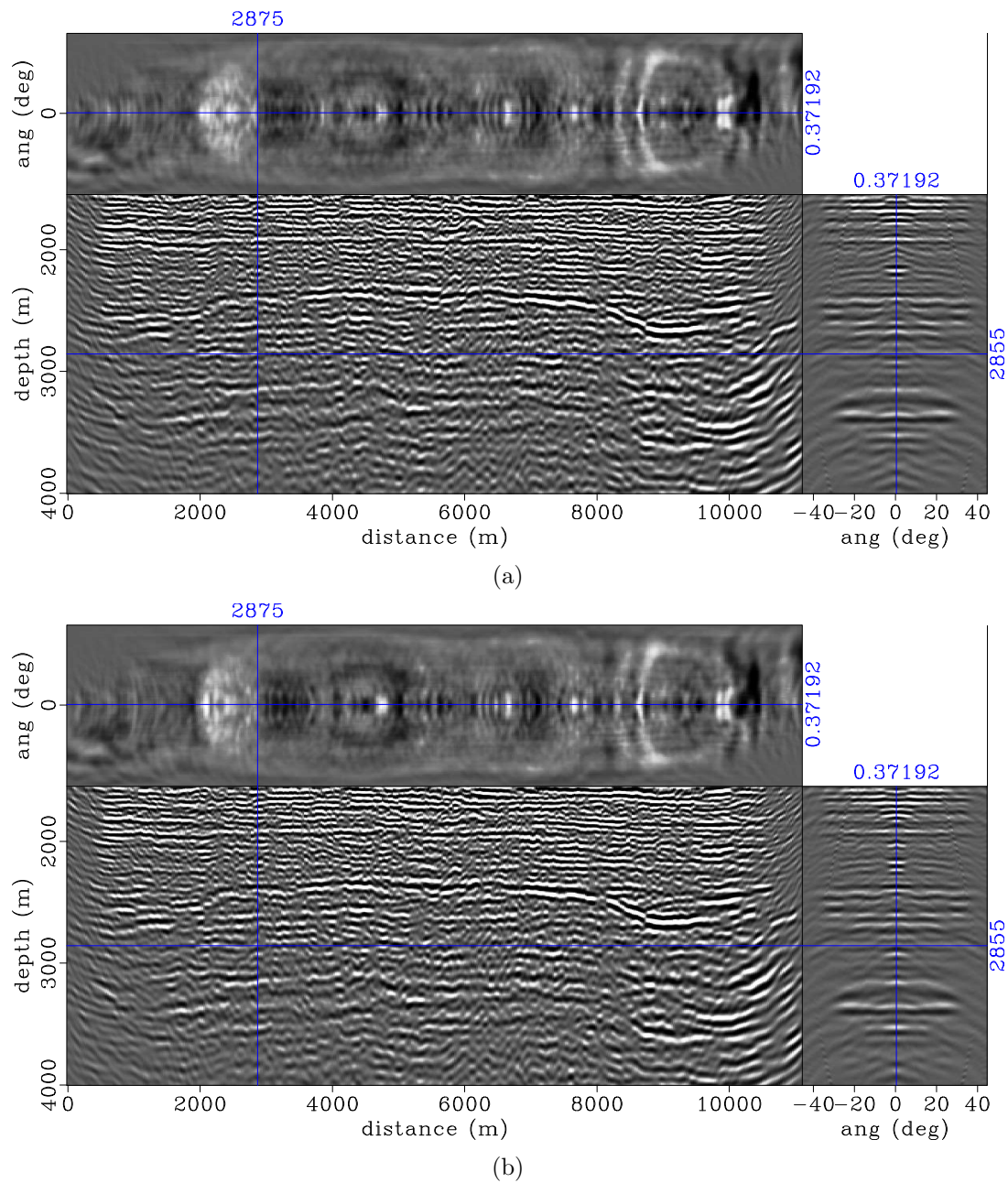
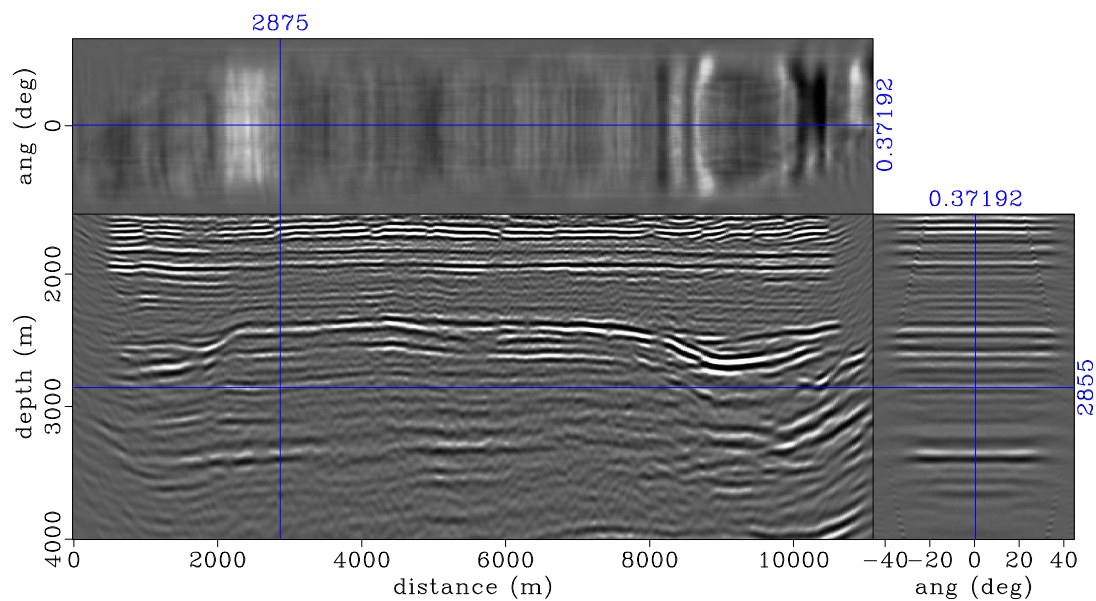
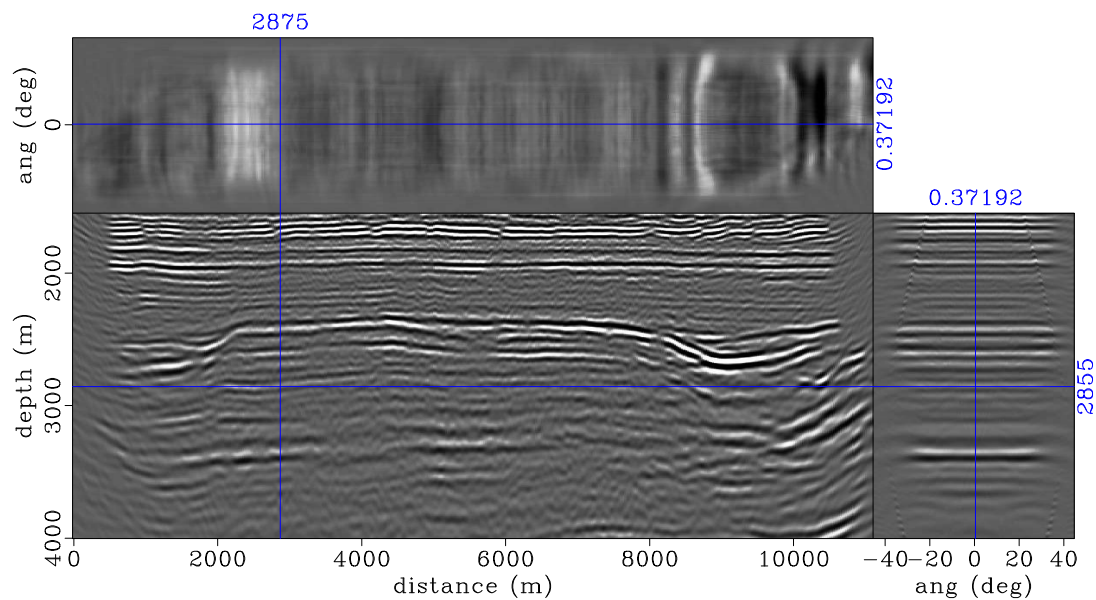


Figure 5.3: Raw pre-stack baseline (a) and monitor (b) images of the target area. In these images, the horizontal events are primaries, which have been adequately imaged. The dominant artifacts in both images are multiples, which show significant curvature across angles. If they are not adequately attenuated, these multiples will contaminate the time-lapse difference between these images. [CR]

chap5/. raw-2759-06,raw-2759-08



(a)



(b)

Figure 5.4: Pre-stack baseline image (a) and monitor image (b) of the target area obtained from the preprocessed data sets. Note that the artifacts in the raw image (Figure 5.3) have been attenuated. In addition, note that the monitor image has been warped (using apparent displacements in Figures 5.5) to the baseline image. [CR]

chap5/. flat-2759-06-s,warp-2759-08

I estimate the amplitude correction as the ratio of the root-mean-square (RMS) energy in the baseline image versus the monitor image:

$$A_m = \frac{E_b}{E_m}, \quad (5.1)$$

where A_m is the amplitude correction term that is applied to the monitor image, E_b is the RMS energy in the baseline image, and E_m is the RMS energy in the monitor image. In this example, I compute this correction term within a 500 m window above the reservoir. I determine that for these images, $A_m = 1.102$ equalizes the energy between the images and attenuates artifacts caused by bulk amplitude differences between them.

Next, to correct for production-induced velocity changes and compaction between surveys, I warp the pre-stack monitor image to the baseline image. Prior to warping the images, to correct for small velocity errors, I first remove any residual moveout in the pre-stack baseline image by aligning all events to the zero-angle image. Then, I compute the apparent displacements between this RMO-corrected baseline image and the monitor image.

Figure 5.5 shows the vertical components of the apparent displacements between these images. These apparent displacements are obtained using the sequential cross-correlation method described in chapter 2. In Figure 5.5, the region with the largest apparent displacements corresponds to the reservoir location. In addition, I observe the presence of a static (almost constant) apparent displacement of approximately 1 m at all image points. This static apparent displacement between the images causes many of the differences between the unaligned images—discussed below. Such displacements may be caused by small changes in the source wavelet, inadequate tidal corrections, or changes in the water velocity.

In order to remove any residual apparent displacements between the stacked baseline and monitor images, using the same sequential warping procedure, I further align these images. However, in this example, the apparent displacements between the stacked images (not shown) are negligible.

Warping the monitor image to the baseline image ensures that all image points become collocated at the baseline position. Because the survey geometries are similar for these surveys, the Hessian matrices for the two aligned images can be approximated by the Hessian matrix obtained with the baseline velocity and geometry.

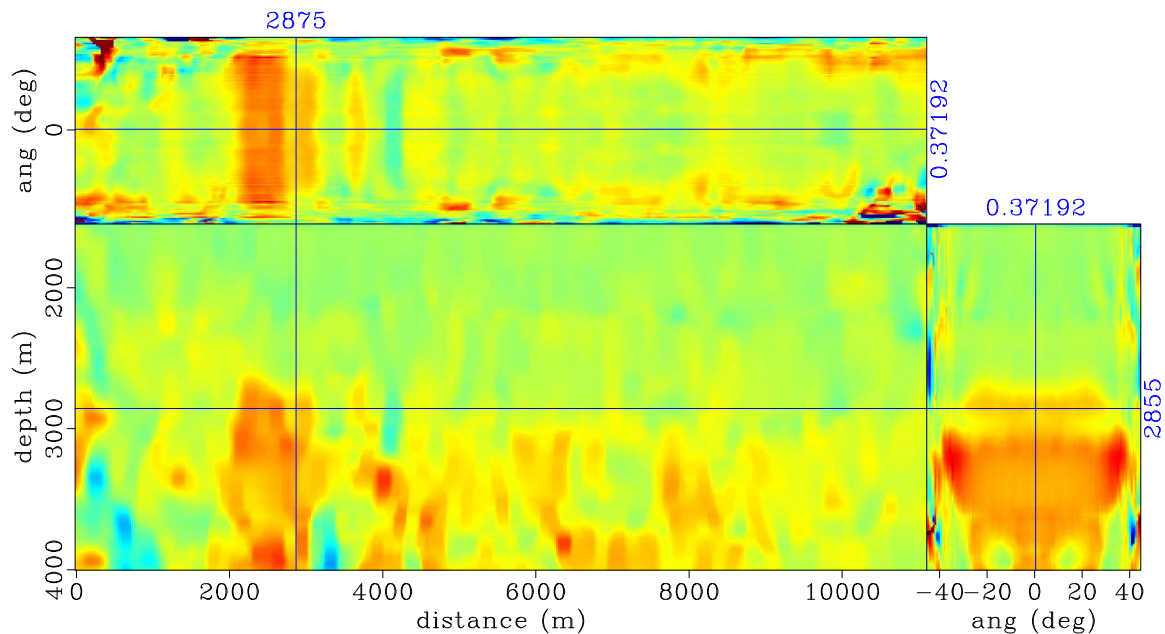


Figure 5.5: Pre-stack apparent vertical displacements between the baseline and monitor images (Figures 5.4(a) and 5.4(b)). Red, blue and green denote positive, negative and zero displacements, respectively. Note that the maximum apparent displacements correspond to the reservoir location in the horizontal range between 2000 m and 3000 m. Also, note that the apparent displacement varies with opening angle.

[CR] chap5/. warp-2759-08-rflat-ts

In this example, I compute the Hessian matrix for the target area using 27 equally spaced frequencies within the frequency band of the data. Because the study area is small, I compute the Green's functions for all surface positions explicitly, and then compute the target-oriented Hessian using the approximation defined in equation 3.10. I compute off-diagonal elements of the Hessian matrix in the range -150 m to $+150$ m along the vertical (depth), and horizontal (common-midpoint) axes. In general, for this example, the Hessian matrix is diagonally dominant.

Figure 5.6 shows the Hessian diagonal (subsurface illumination) for the target area. Note that for this complete geometry, because of the relatively simple overburden geology, the estimated subsurface illumination is well-behaved, with gradually decreasing illumination with depth. An example of the off-diagonal elements of this Hessian at a sample sub-surface location, represented as elements of the PSF at that location, is shown later in the chapter (Figure 5.13).

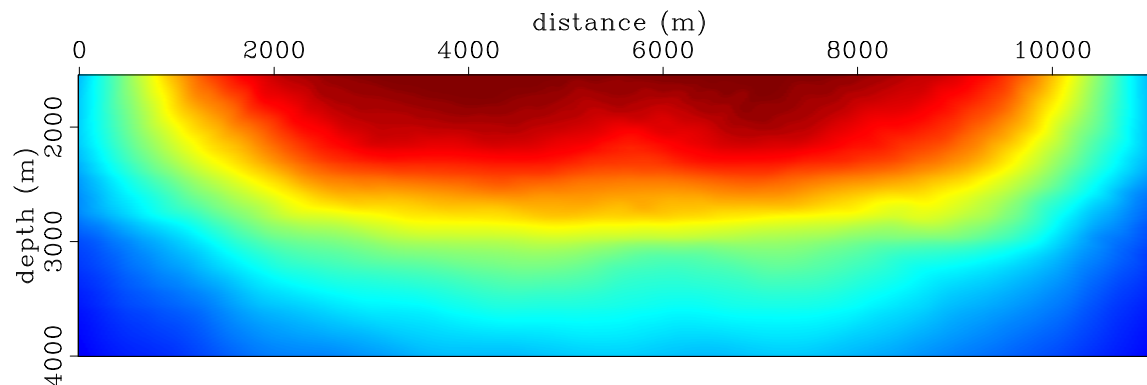


Figure 5.6: Hessian diagonal (subsurface illumination) for the target area. Red indicates regions with high illumination, whereas blue indicates regions with low illumination. [CR] chap5/. hs-06

The spatial regularization operator used in this example is constructed from non-stationary dip-filters derived from factorized directional Laplacians (Hale, 2007). Figure 5.7 shows the local dips obtained from the stacked preprocessed baseline image using the plane-wave destruction method (Fomel, 2002). Because both images have been aligned by prior to inversion, I use the same spatial regularization operator for both of them. As in chapter 4, the temporal regularization in the inversion is a difference operator applied to the images. This provides coupling between the inverted images and ensures that there are only limited differences between them.

Figure 5.8 shows the migrated time-lapse image from the raw data, after Radon demultiple, and after amplitude balancing. Figure 5.9 shows the same image after pre-stack warping, after residual post-stack warping, and after inversion. Note that the raw migrated time-lapse image contain several artifacts that are not associated

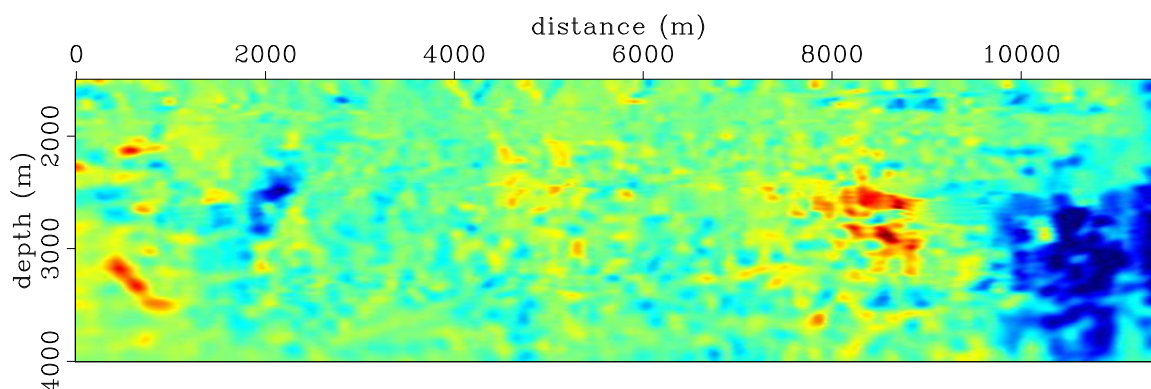


Figure 5.7: Dips derived from the stacked baseline image. Red indicates positive dips, whereas blue indicates negative dips. These dips are used to construct the spatial regularization operator used in the inversion. [CR] chap5/. dm-dip-2759

with production-induced changes in the reservoir properties (Figure 5.8(a)). Note the incremental improvements in the time-lapse image quality after different preprocessing steps and after inversion.

In Figure 5.8(b), note that the multiple attenuation step described above has reduced most of the incoherent artifacts in the time-lapse image. Furthermore, by balancing the RMS energy between the baseline and monitor images, differences between them are reduced further (Figure 5.8(c)). Importantly, a comparison of the time-lapse images in Figures 5.8(c) and 5.9(a) shows that the biggest improvements in the time-lapse image-quality are after removal of the static and dynamic displacements by warping the monitor image to the baseline image. For example, the strong artifact in the time-lapse image around 9,000 m, which is caused by differencing two misaligned large amplitude events in the baseline and monitor images, have been removed after warping. Furthermore, geologically consistent artifacts, which are caused by the static displacement between the images, have been attenuated. As described above, in this example, residual warping of the stacked images provides only limited improvements to the time-lapse image (Figure 5.9(b)).

Finally, because inversion attenuates most of the residual artifacts between the images, the quality of the time-lapse image is improved further (Figure 5.9(c)).

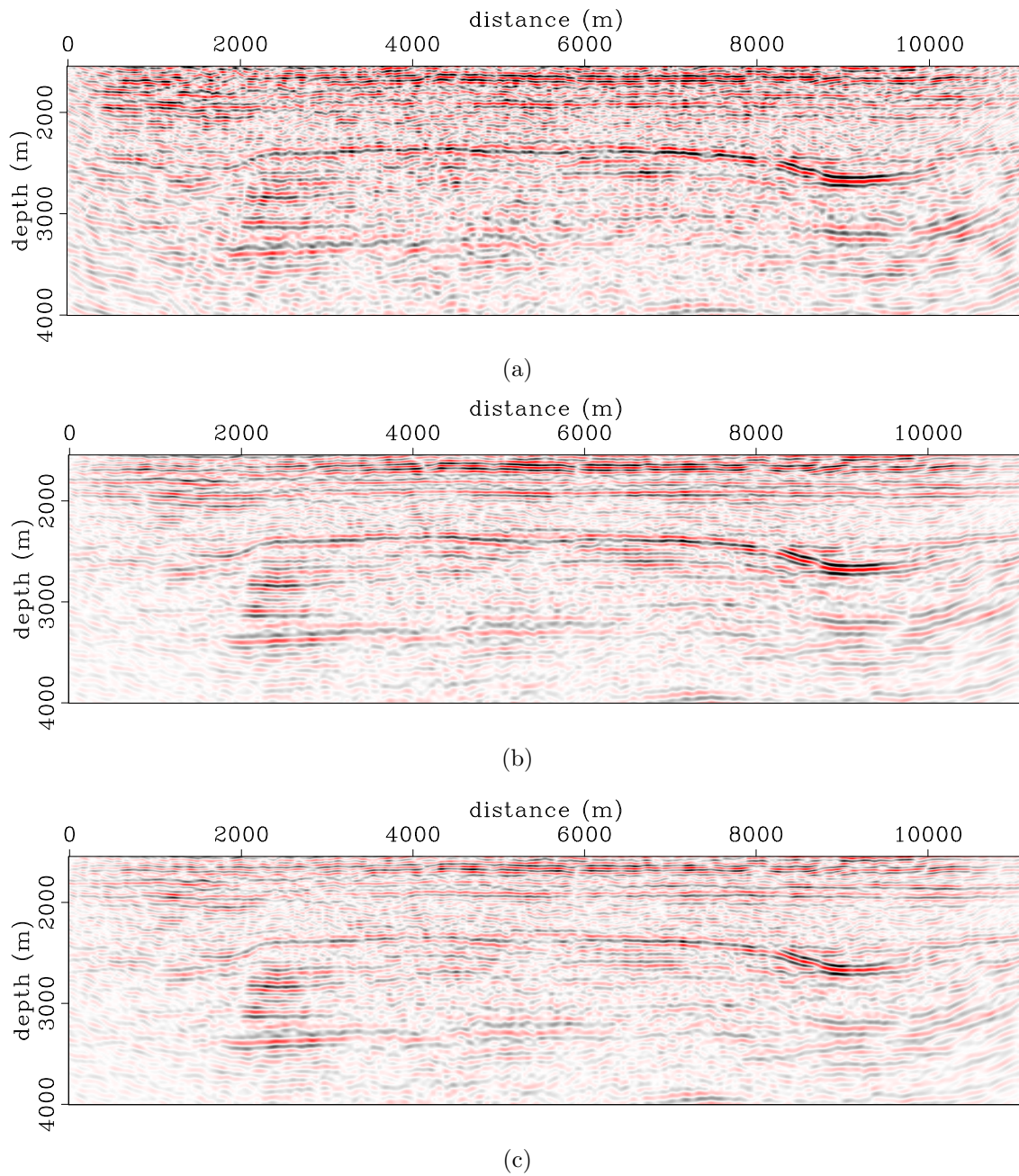


Figure 5.8: Time-lapse images obtained from the raw data (a), after multiple attenuation by parabolic Radon demultiple (b), and after amplitude correction (c). Note the incremental improvements in the time-lapse image from (a) to (c). [CR]

chap5/. raw-2759-4d,dmult-2759-4d,amp-2759-4d

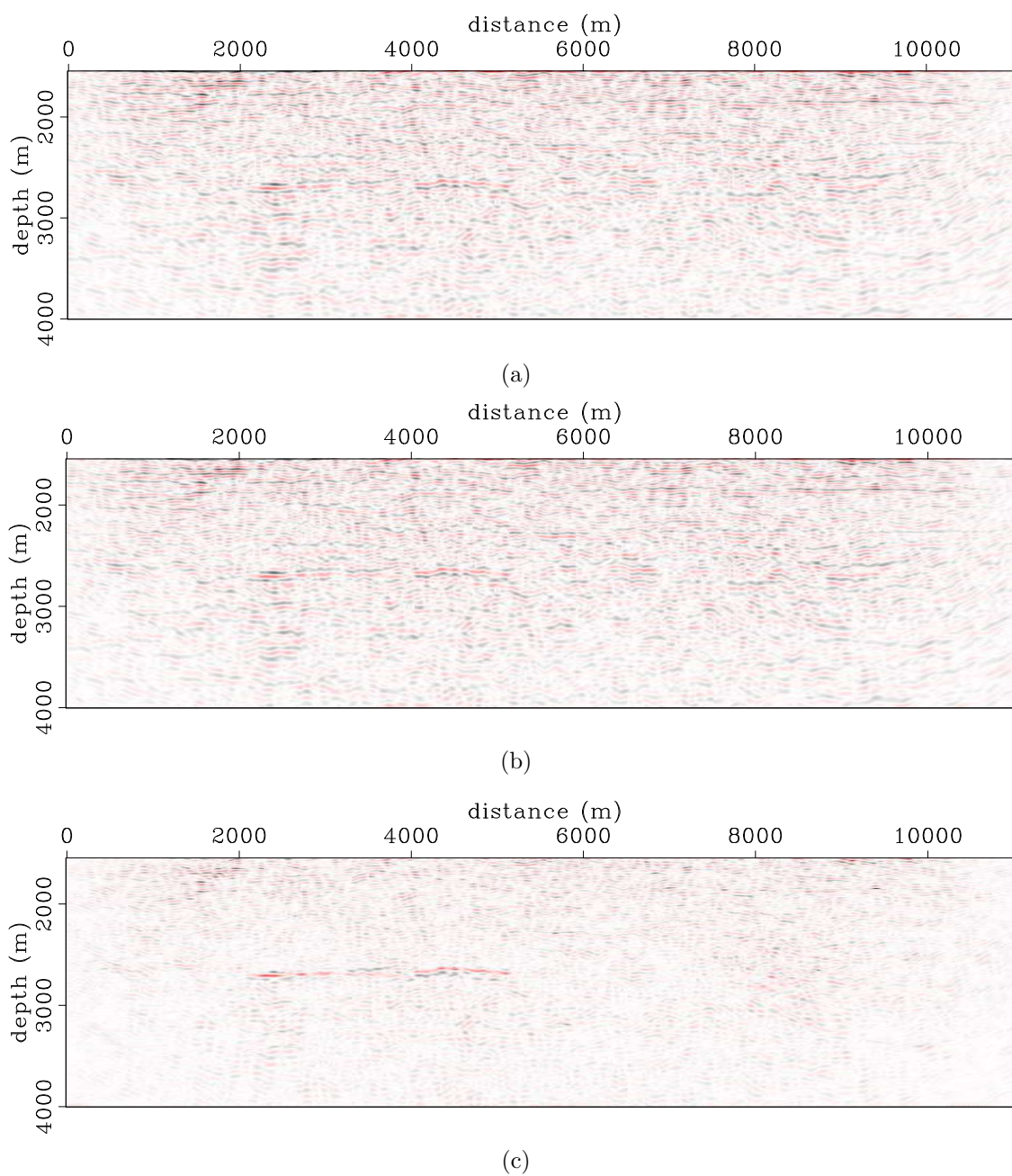


Figure 5.9: Time-lapse images obtained after pre-stack warping (a), after residual post-stack warping (b), and after image-domain inversion (c). Note the incremental improvements in the time-lapse image from (a) to (c). [CR]

chap5/. warp-2759-4d,rwarp-2759-4d,inv-2759-4d

Example II: Inversion of incomplete data sets

In this example, I present the preprocessing and inversion of the complete baseline and incomplete monitor data sets. As previously stated, I simulate an obstruction in the monitor geometry such that neither sources nor receivers are present between 2500 and 2900 m. Apart from the presence of this gap in the monitor geometry, the baseline and monitor geometries in this example are the same as those used in example *I*.

Figure 5.10 shows a portion of the gapped monitor data. Note that the gap in this data set is located directly above the area of interest. In this example, the preprocessing steps and migration parameters are the same as those used in example *I*. However, there are some differences necessitated by the obstruction in the monitor geometry. First, the multiple attenuation requires a mask that accounts for the presence of the gap in the monitor data. This ensures that this gap does not affect the estimated Radon model. The masking operator is a diagonal operator with zeros in the gap area and ones at all other locations.

Second, to obtain the amplitude correction, as in example *I*, I utilize a window above the reservoir, but in parts of the image unaffected by the gap in the monitor geometry. This ensures that the measured difference in RMS amplitudes is not caused by the gap in the monitor geometry. As in the previous example, I obtain an amplitude correction $A_m = 1.102$.

Third, in order to align events in this incomplete monitor image to the complete baseline image, I first perform interpolation to fill in the hole in the monitor data. As in the multiple attenuation step, this interpolation operator is a parabolic Radon function. The interpolated monitor data (not shown) are then imaged and processed using the same parameters as in the complete monitor case. The resulting pre-stack image is then used to estimate the apparent displacement vectors that are used to warp the incomplete monitor image to the baseline. This approach ensures that the pre-stack baseline and monitor images have similar kinematics, and ensures more reliable estimates of the apparent displacements between the migrated images.

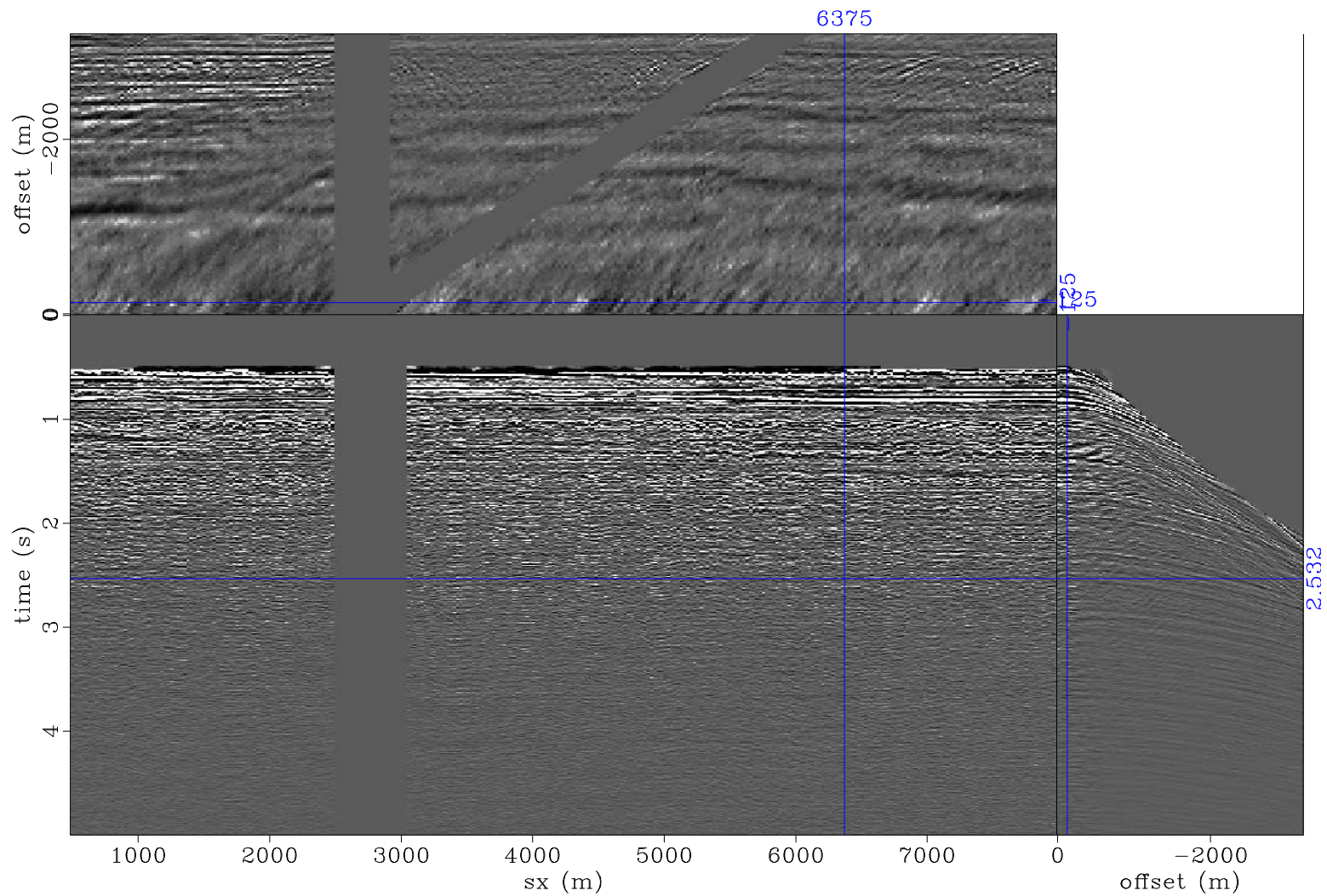


Figure 5.10: Gapped monitor data. Note that sources and receivers are missing within the simulated obstruction.
 [CR] chap5/. dmhl-dat-2759-b4-hole

Figure 5.11 shows the vertical components of the apparent displacements between the baseline and monitor images. Note that these apparent displacements are comparable to those obtained in example *I* (Figure 5.5). As in example *I*, in this image, the region with the largest apparent displacements correspond to the reservoir location.

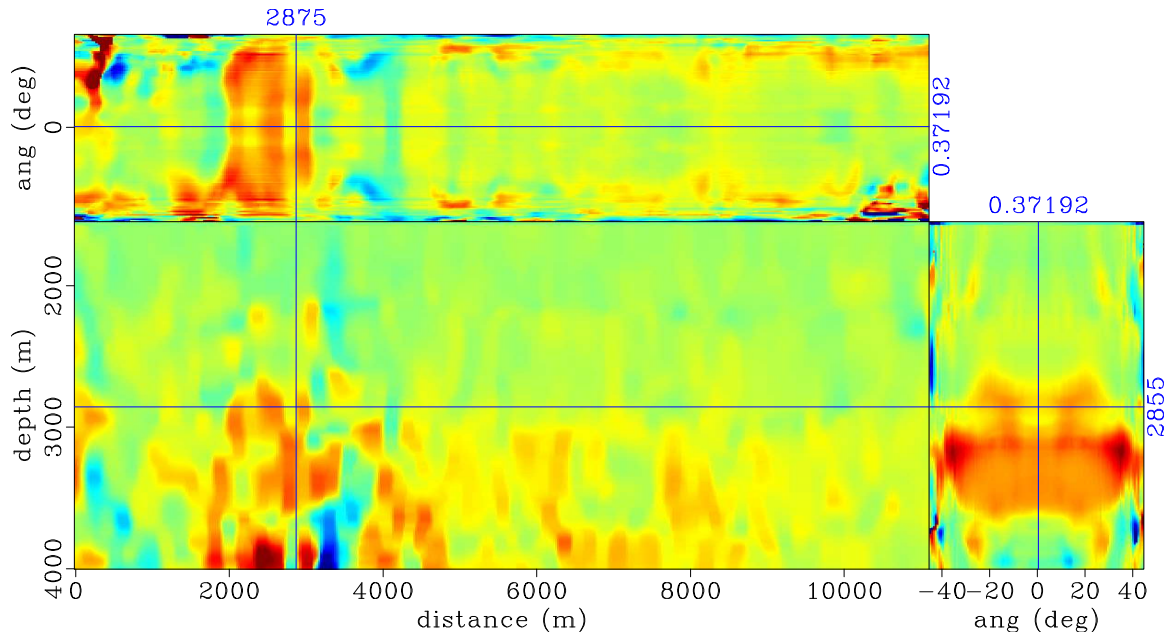


Figure 5.11: Pre-stack apparent vertical displacements between the complete baseline image and the image from interpolated monitor data sets. Comparing this to Figure 5.5, note that estimates of the apparent displacements are similar to those from the complete data case. [CR] chap5/. dmhl-warp-2759-08-rflat-ts

I compute the Hessian for the incomplete monitor geometry with the same parameters used for the complete baseline geometry in example *I*. The illumination ratio between the baseline and monitor geometries (monitor illumination divided by baseline illumination) is shown Figure 5.12. Note that, in general, regions of the subsurface that are imaged with the same survey geometries have similar illumination, and hence the illumination ratio equals unity. Regions of the subsurface that are imaged with different geometries have different illumination, and hence illumination ratios in these regions are less than unity. In this example, the region with low illumination ratios corresponds to parts of the subsurface that are affected by the

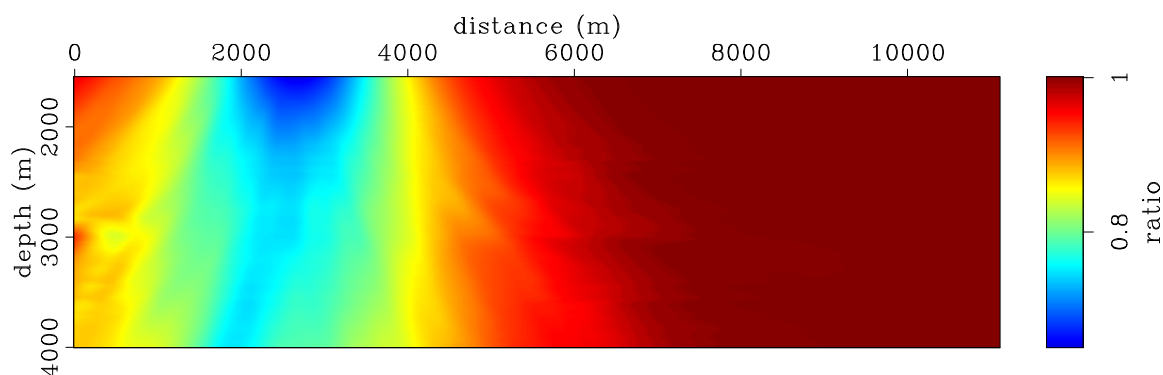


Figure 5.12: Illumination ratio between the baseline and monitor. Red indicates regions with equal illumination (i.e., ratio equals unity) whereas blue indicates unequal illumination (i.e., ratio less than unity). [CR] chap5/. hs-rat

simulated obstruction in the monitor geometry (Figure 5.12). Note that this region also corresponds to the reservoir location.

Figure 5.13 shows the spatial- and wavenumber-domain point-spread functions at point $x = 2600$ m and $z = 2600$ m. Because of the gap in the monitor geometry, as expected, a comparison of the two PSFs shows that this image point is illuminated with a lower seismic energy in the monitor survey than in the baseline. Figure 5.14 shows the differences in the PSFs in the spatial and wavenumber domains. The difference in geometry leads to significant differences off-diagonal elements (i.e., points away from the central point of the spatial PSF). These differences are equivalent to differences in the ranges of illuminated wavenumbers for the two geometries (Figure 5.14(b)).

Figure 5.15 shows the time-lapse images obtained after different processing steps. Note the incremental improvements in the time-lapse image quality after processing and after inversion. In Figure 5.15(a), in addition to artifacts present in the raw time-lapse image in example I (Figure 5.8(a)), high-amplitude artifacts are also present in parts of the image below the obstruction. Because of these artifacts, compared to the complete data example (Figure 5.9(b)), the time-lapse image from conventional processing (Figure 5.15(b)) is of poorer quality. These artifacts have been attenuated in the inverted time-lapse image (Figure 5.15(c)).

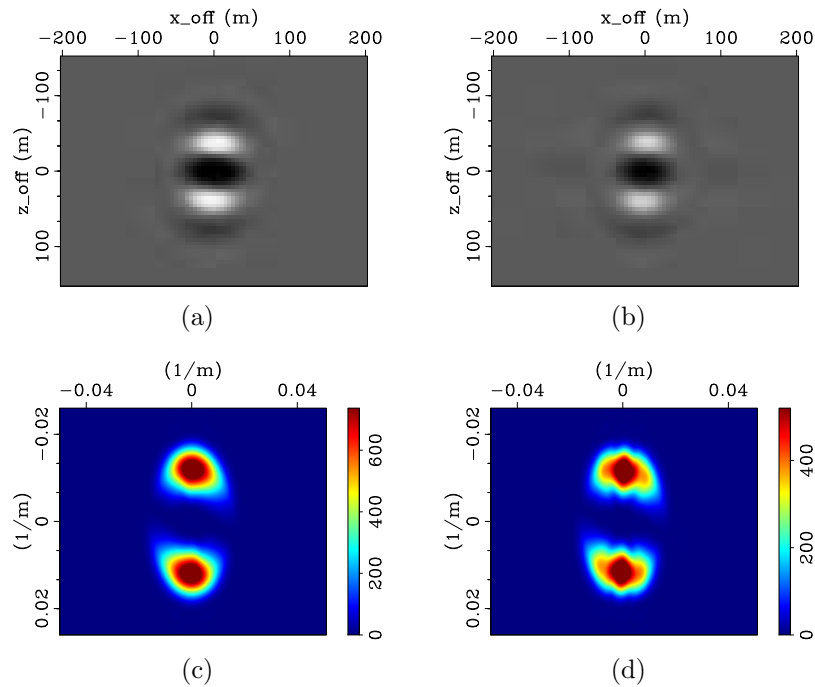


Figure 5.13: PSFs at point $x = 2600$ m and $z = 2600$ m for the baseline (a) and (c), and the monitor (b) and (d). The panels show the PSFs in the spatial domain (a) and (b), and in the wavenumber domain (c) and (d). The differences between these PSFs are shown in Figures 5.14. [CR] chap5/. hs-offd-06,hs-offd-08,hs-fft-06,hs-fft-08

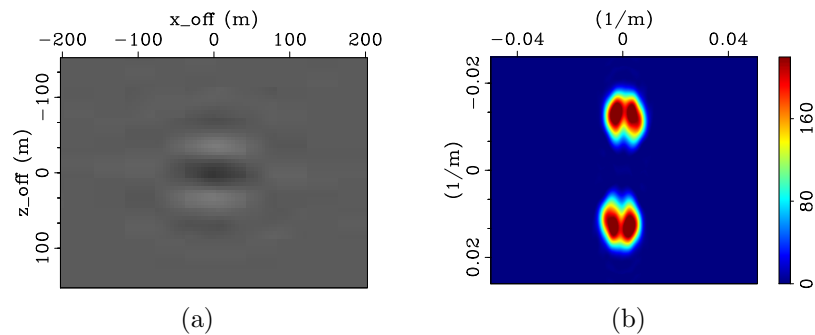


Figure 5.14: Differences between the baseline and monitor PSFs at $x = 2600$ m and $z = 2600$ m in the spatial domain (a) and wavenumber domain (b). In (a), note that there are significant differences between PSFs away from the central point (i.e., in the off-diagonal elements of the Hessian matrices). Likewise, in (b), there are significant differences in wavenumber illumination for the two geometries. [CR] chap5/. hs-offd-diff,hs-fft-diff

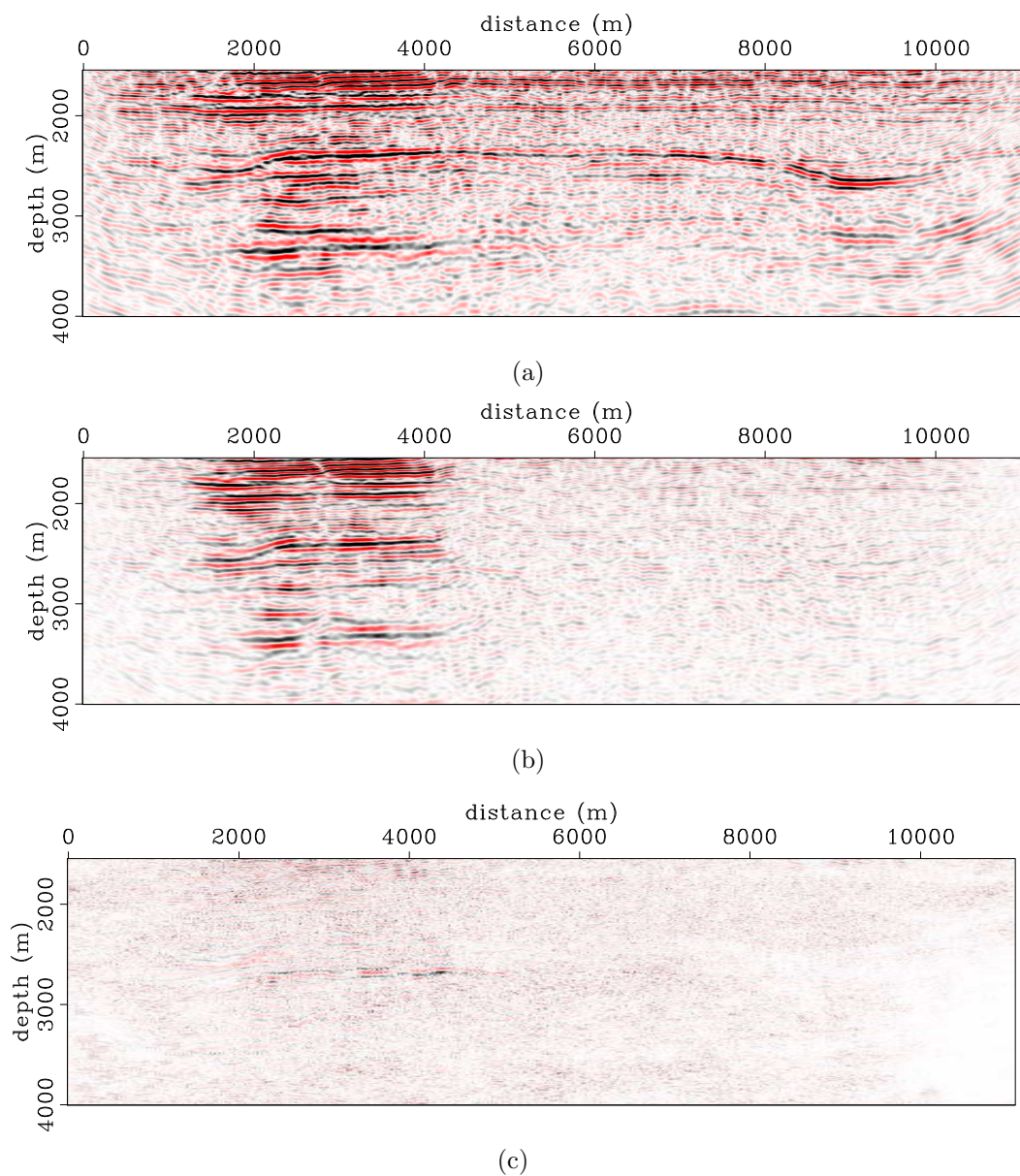


Figure 5.15: Time-lapse images obtained from the raw data (a), after conventional time-lapse processing (b), and after image-domain inversion (c). Because of artifacts introduced by the incomplete monitor data, conventional methods fail to provide results of comparable quality to the complete data example (Figure 5.9(b)). As shown in (c), regularized joint inversion provides satisfactory results. [CR]

chap5/. dmhl-raw-2759-4d,dmhl-rwarp-2759-4d,dmhl-inv-2759-4d

One common way to account for subsurface illumination variations in migrated images is through weights defined as the inverse of the diagonal of the Hessian (Plessix and Mulder, 2004; Etgen et al., 2009). Approximating the Hessian matrix by its diagonal assumes that at any subsurface point, all illuminated wavenumbers/angles should be weighted equally by the value of the Hessian diagonal. For the time-lapse problem, this approximation is sufficient if the acquisition geometries—and hence, differences in the properties of the Hessian matrices—for different surveys are similar. However, where the geometry differences are large, the diagonal of the Hessian is a poor approximation. For example, Figure 5.16 shows the time-lapse

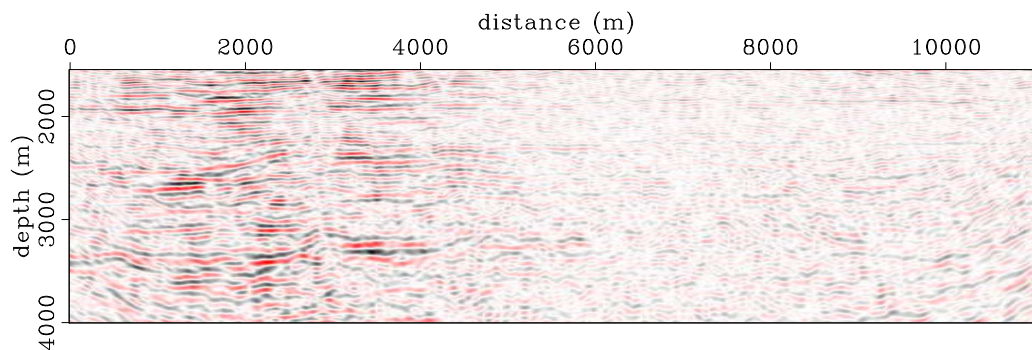


Figure 5.16: Time-lapse image obtained after weighting the baseline and monitor images by the diagonal of the Hessian matrices. Because the diagonal of the Hessian does not contain full information about subsurface illumination discrepancies, it only provides limited improvements compared to conventional methods (Figure 5.15(b)). As shown in Figure 5.15(c), regularized joint inversion provides a time-lapse image that is more comparable in quality to the complete data example (Figure 5.9(b)).

[CR] chap5/. dmhl-dinv-2759-4d

image derived as the difference between the weighted migrated images derived from the complete baseline and incomplete monitor data sets. Although, compared to the time-lapse image from the unweighted migrated images (Figure 5.15(b)), this image contains fewer artifacts, it is of poorer quality than the image derived from regularized inversion (Figure 5.15(c)).

Discussion

Example *I* demonstrates that in order to obtain reliable estimates of the production-related changes in time-lapse seismic data sets, even where the data are acquired with state-of-the-art methods, careful data preprocessing is necessary. In addition to improving the quality of time-lapse amplitude information, these preprocessing steps are required to ensure that the data satisfy sufficiently the primaries-only assumption in the inversion formulations.

First, using a parabolic Radon operator, multiples and other artifacts in the raw data are attenuated. Compared to the pre-stack images obtained from the raw time-lapse data (Figures 5.3), the preprocessed pre-stack images contain significantly fewer artifacts (Figure 5.4). In addition, because of small differences in the acquisition instruments, there is a bulk amplitude difference between the baseline and monitor images. Amplitudes between the baseline and monitor images are sufficiently balanced by multiplying the monitor image by the ratio of the RMS energy between the migrated images outside the reservoir region.

In this example, by first warping the images prior to stacking, I ensure that image defocusing—due to production-induced velocity changes and compaction—is minimized. In addition, warping provides a way to remove the static apparent displacements of approximately 1 m between the baseline and monitor images. As previously discussed, in this example, these static displacements may have been caused by small changes in the source wavelet, inadequate tidal corrections, or changes in the water velocity. The sequential one-dimensional warping method described in chapter 2 provides an efficient way to align these pre-stack images. Because the overburden geology along the studied section is relatively simple, the baseline image (Figure 5.4(a)) and the monitor image (Figure 5.4(b)) are sufficiently aligned using only vertical components of the prestack apparent displacement vectors (Figure 5.5). The apparent displacements between the stacked baseline and monitor images are negligible.

As shown in the Figure 5.8(a), even with good repeatability between survey geometries, it is often impossible to interpret an unprocessed time-lapse image. However,

after careful processing, it is possible to make meaningful interpretations of amplitude information in the time-lapse image (Figure 5.9(b)). Although in many cases, results obtained from a conventional processing workflow may suffice, the quality of the time-lapse image can be improved by inversion (Figure 5.9(c)).

In example *II*, the simulated obstruction in the monitor geometry represents a practical problem in many field applications, where the construction of production facilities causes differences between the baseline and monitor geometries. As discussed earlier in this dissertation, if such differences are small, data-regularization methods (e.g., interpolation) may be sufficient to correct for them. However, although the time-lapse amplitude information derivable from the interpolated monitor data (not shown) is of poor quality, the kinematics of the monitor image are similar to those of the complete baseline image. Therefore, these provide adequate estimates of the warping parameters (Figure 5.11) that are comparable to those from the complete data case (Figure 5.5).

Because the monitor data is incomplete, the effective geometries differ for the two surveys, thereby leading to illumination mismatch (i.e., illumination ratios less than unity) in parts of the target area (Figure 5.12). However, the Hessian diagonal gives only a partial measure of the illumination mismatch between time-lapse surveys (Figure 5.12). Large geometry differences (e.g., an obstruction in the monitor acquisition) can cause large differences in the off-diagonal elements of the Hessian (Figures 5.13 and 5.14). As a consequence, as shown in Figures 5.13 and 5.14, such geometry differences lead to differences in the range of illuminated wavenumbers/angles between surveys. Therefore, a point-by-point amplitude compensation using only the Hessian diagonal is inadequate.

In this example, artifacts in Figure 5.15(a), caused by the large differences in acquisition geometries between the baseline and monitor surveys, cannot be adequately attenuated by conventional time-lapse processing methods (Figure 5.15(b)). In this case, regularized joint image-domain inversion provides a significant improvement to the time-lapse image (Figure 5.15(c)). Finally, as shown in figure 5.16, because it contains only limited information about subsurface illumination discrepancies, the

diagonal of the Hessian cannot fully account for the effects of geometry differences between time-lapse seismic data sets.

CONCLUSIONS

Careful data preprocessing is an important part of time-lapse seismic imaging—even more when performing inversion, as processed in this dissertation. In this chapter, I showed how data preprocessing helps to remove uncorrelated artifacts and multiples in the recorded data. In addition, I showed that it helps to account for small differences in recording equipment and environmental conditions for different surveys. And, importantly, I showed that these preprocessing steps can be used to condition the recorded data for regularized joint inversion.

For data sets recorded with carefully repeated conventional acquisition geometries, the preprocessing methods described in this chapter can provide time-lapse images that are representative of the actual changes in reservoir properties. However, where there are significant differences between the acquisition geometries of different surveys, these preprocessing methods are insufficient. This is because differences in acquisition geometries cause differences in the range of illuminated wavenumbers/angles at subsurface image points. Because regularized joint image-domain inversion accounts for such illumination mismatches and for band-limited wave-propagation effects, it provides images with improved resolution and better definition of seismic amplitude changes.

In the next chapter, I demonstrate different applications of regularized joint inversion to three-dimensional ocean-bottom-cable (OBC) time-lapse data sets.

ACKNOWLEDGMENTS

I thank Statoil and partners (ENI and Petoro) for donating the Norne data. I thank the Stanford Center for Computational Earth & Environmental Science (CEES) for providing the computer resources used in these studies.